



Nanoscale

**First-principles calculations for understanding the  
microstructures and mechanical properties of co-sputtered  
Al alloys**

Journal:	<i>Nanoscale</i>
Manuscript ID	NR-ART-05-2021-003333.R1
Article Type:	Paper
Date Submitted by the Author:	11-Aug-2021
Complete List of Authors:	Gong, Mingyu; University of Nebraska-Lincoln Wu, Wenqian; University of Nebraska-Lincoln Xie, Dongyue; University of Nebraska-Lincoln, Mechanical and Materials Engineering Richter, Nicholas; Purdue University Li, Qiang; Purdue University, Materials engineering Zhang, Yifan; Purdue University xue, sichuang ; Purdue University System, MSE Zhang, Xinghang; Purdue University System, Materials Engineering Wang, Jian; University of Nebraska-Lincoln College of Engineering, Materials Engineering

SCHOLARONE™  
Manuscripts

## First-principles calculations for understanding the microstructures and mechanical properties of co-sputtered Al alloys

Mingyu Gong<sup>a</sup>, Wenqian Wu<sup>a</sup>, Dongyue Xie<sup>a</sup>, Nicholas A. Richter<sup>b</sup>, Qiang Li<sup>b</sup>, Yifan Zhang<sup>b</sup>,  
Sichuang Xue<sup>b</sup>, Xinghang Zhang<sup>b</sup>, Jian Wang<sup>a,\*</sup>

<sup>a</sup> Mechanical and Materials Engineering, University of Nebraska-Lincoln, Lincoln, NE 68588, USA

<sup>b</sup> School of Materials Engineering, Purdue University, West Lafayette, IN 47907, USA.

\* Corresponding author: Jian Wang (jianwang@unl.edu)

### Abstract

Recent experimental studies show that co-sputtering solutes with Al together can refine columnar grain size around few tens nanometers and promote formation and enhance the stability of planar defects such as stacking faults (SFs) and grain boundaries (GBs) in Al alloys. These crystal defects and fine columnar grains result in high strength, enhanced strain hardening and thermal stability of these Al alloys. Using first-principles density-functional theory (DFT) calculations, we studied the role of eleven solutes in tailoring kinetics and energetics of adatoms and clusters on Al {111} surface, stable and unstable stacking fault energies, and kinetic energy barriers for defects migration. The calculations show that most solutes can effectively refine columnar grain size through decreasing diffusivity of adatoms and surface clusters. These solutes do not necessarily decrease the stacking fault energy of Al alloys, but reduce the formation energy of faulted surface clusters and increase the energy barriers for the recovery of faulted surface clusters. Correspondingly, the formation of SFs is kinetically promoted during sputtering. Furthermore, solutes are segregated into the core of Shockley partial dislocations and play pinning effect on SFs, SF arrays and twin boundaries, enhancing thermal stability of these crystal defects. These findings provide insights into design of high-strength Al alloys for high temperature applications.

**Keywords:** Al, impurity, kinetics and energetics, density-functional theory.

## 1. Introduction

Mechanical properties of a material, such as strength, ductility and elastic modulus, are determined by the constituent phase and microstructure, which can be modified by their compositions and the synthesizing and forming processes. Generally, plastic deformation associated with generation and reaction of crystal defects changes grain size and texture<sup>1-5</sup>, while heat treatments further modify microstructure including grain size, texture and formation of secondary phases<sup>1, 6-11</sup>. Sputtering techniques with unique growth kinetics associated with surface diffusion can tailor microstructures and composition through controlling deposition conditions<sup>12-16</sup>. Differing from bulk crystals, the spatial distribution and forms of solutes in sputtered materials could be far-from equilibrium state due to surface kinetics<sup>17</sup>.

Aluminum (Al) alloys have wide applications in automobile and aerospace industries due to their competitive strength-to-weight ratio<sup>18, 19</sup>. Typical strengthening mechanisms include secondary phase<sup>20-22</sup>, grain refinement<sup>23, 24</sup>, solid solution strengthening<sup>25, 26</sup> and so on. For example, Al-Mg alloys prepared by cryomilling have an average grain size of 26 nm, and a flow stress of 750 MPa<sup>23</sup>. However, Al alloys cannot be continuously strengthened by refining grain size because grain boundary (GB)-mediated activities, such as grain coarsening and GB sliding/migration, become dominant when grain size is smaller than a critical value<sup>27-29</sup>. Moreover, high-angle GBs store high energy<sup>30-32</sup>, causing a low thermal stability of the fine grains. Microstructure can be stabilized by solute segregation induced pinning on GBs<sup>33-35</sup> and/or forming low energy GBs, such as twin boundaries (TBs)<sup>36-38</sup>. High density of stacking faults (SFs) and coherent TBs (CTBs) have been observed in nanotwinned (nt) metals and alloys with low or medium intrinsic stacking fault energy (SFE), such as nt Ag<sup>39</sup> (with 16 mJ/m<sup>2</sup> SFE), nt Cu<sup>40</sup> (with 41 mJ/m<sup>2</sup> SFE) and nt Ni<sup>41</sup> (with 90 mJ/m<sup>2</sup> SFE). However, it is hard to introduce high density of twins in Al with high SFE (120-166 mJ/m<sup>2</sup>)<sup>42</sup> by mechanical deformation. Through co-sputtering metal solutes with Al together (referred to as Al-X), we have prepared seven binary Al alloys with profuse nanotwinned columnar structures, SFs and twins in each column<sup>43-53</sup>. More importantly, these Al-X alloys exhibit high strengths, enhanced strain hardening and good thermal stability.

For co-sputtered Al-X alloys, high strength and enhanced strain hardening can be ascribed to fine grain size, high density of planar defects, and nanotwins while the good thermal stability arises from high kinetic energy barriers for the recovery/motion of these crystal defects. We speculate

several reasons for producing and stabilizing such microstructures corresponding to deposition process: addition of solutes may reduce the SFE of Al; solutes on surface may modify kinetics and energetics for adatoms and clusters on surface; and solutes may stabilize the microstructures including Shockley partial dislocations, twin boundaries and grain boundaries via modification of kinetic energy barriers for defect motion. However, a solid understanding on the formation and stabilization of such microstructures remains missing. In this work, we aim at exploring the role of impurity in tailoring microstructures and mechanical properties of co-sputtered Al-X alloys based on first-principles density-functional theory calculations and collected experimental results.

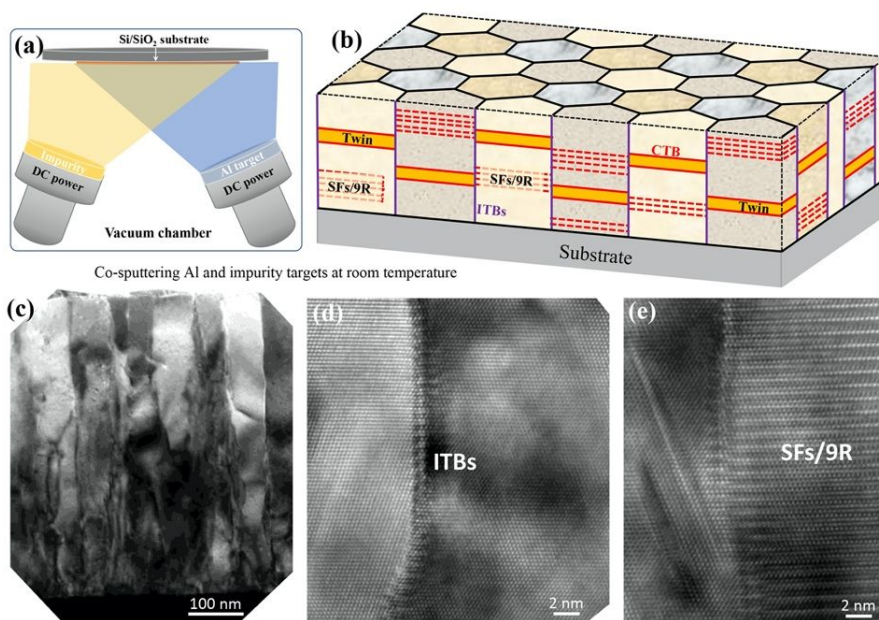


**Fig. 1** (a) Schematics showing synthesis of Al and Al alloy film using co-sputtering. (b) Schematics showing columnar microstructures with in-column nanotwins, SFs and 9R phase bands of sputtered Al and Al-X alloys. Microscopy observations of (c) columnar microstructures, (d) ITBs between two grains and (e) in-column SFs and 9R phase bands in Al-5Mg films.

## 2. Key experimental findings of sputtered Al alloys

Pure Al and binary Al-X alloy films were sputter-deposited (Fig. 1(a)) at room temperature using DC magnetron sputtering<sup>43-60</sup>. The base pressure before deposition was around  $0.5-1.0 \times 10^{-7}$  torr and the Ar pressure was  $1 \times 10^{-3}$  torr. The deposition rate was in the range of 0.35-0.45 nm/s. Here, we summarize the key experimental data (microstructures and mechanical properties) of pure Al<sup>43-45</sup>, co-sputtered Al-Mg<sup>46</sup>, Al-Ti<sup>47</sup>, Al-Fe<sup>48, 49</sup>, Al-Co<sup>50</sup>, Al-Ni<sup>51, 52</sup>, Al-Zr<sup>53</sup> and Al-

Ag<sup>49</sup> alloy films. For consistency and simplicity, sputtered Al-X alloy film with  $m$  at.% solute is referred to as Al- $m$ X alloy.

When solute concentration is less than 10 at.%, sputtered Al-X alloys have columnar microstructures as schematically shown in Fig. 1(b). Fig. 1(c)-(e) are typical transmission electron microscopy (TEM) images showing cross-sectional view of the sputtered Al alloys. Several microstructural features are briefly summarized. First, most sputtered Al-X alloys have columnar structures with strong {111} texture along the growth direction. Second, the energy-dispersive X-ray spectroscopy (EDS) confirms that all as-deposited Al-X alloys form the complete solid solution without secondary phases. Third, these columns hold the twin orientation, and thus these Al-X alloys are referred to as nanotwinned (nt) Al-X alloys. Corresponding to the twin orientation between columns, GBs are likely to have the character of {112} incoherent twin boundaries (ITBs)<sup>61</sup>. Fourth, in general, a greater solute concentration leads to smaller columnar grain sizes in Al-X alloys. Fig. 2(a) shows the normalized columnar grain sizes for Al-X alloys ( $d_{\text{Al-X}}/d_{\text{Al}}$ ) with respect to solute concentration. The average columnar grain size of sputtered pure Al,  $d_{\text{Al}}$  is about 450 nm. It is noted that the average columnar grain size of Al-Ag alloys is greater than pure Al. Fifth, many columns contain nanotwins and 9R phase bands, being referred to as twinned columnar structure, as revealed by microscopy studies and X-ray diffraction (XRD) pole figure analyses. It is noted that Al-Ag alloys are an exception because no twinned columnar structures form. For several nt Al alloys, statistics of 9R phase bands were reported in few works<sup>49, 51, 53</sup>. Li *et al.*<sup>49</sup> reported that the volume fraction of 9R phase in Al-2.5Fe is 25%, much greater than that in sputtered Al. Assuming the volumetric ratio of 9R phase in each column in Al-2.5Fe alloy is less than 50%, the fraction of columns containing 9R phase could be more than 50%. Fig. 2(b) plots the fraction of columns containing 9R phase with respect to solute concentration in nt Al-Fe<sup>49</sup>, Al-Ni<sup>51</sup> and Al-Zr<sup>53</sup> alloys. With the same concentration, Zr solutes can induce more 9R phase than Ni solutes. Also, it can be speculated that Fe solutes can induce more 9R phase than Zr solutes.

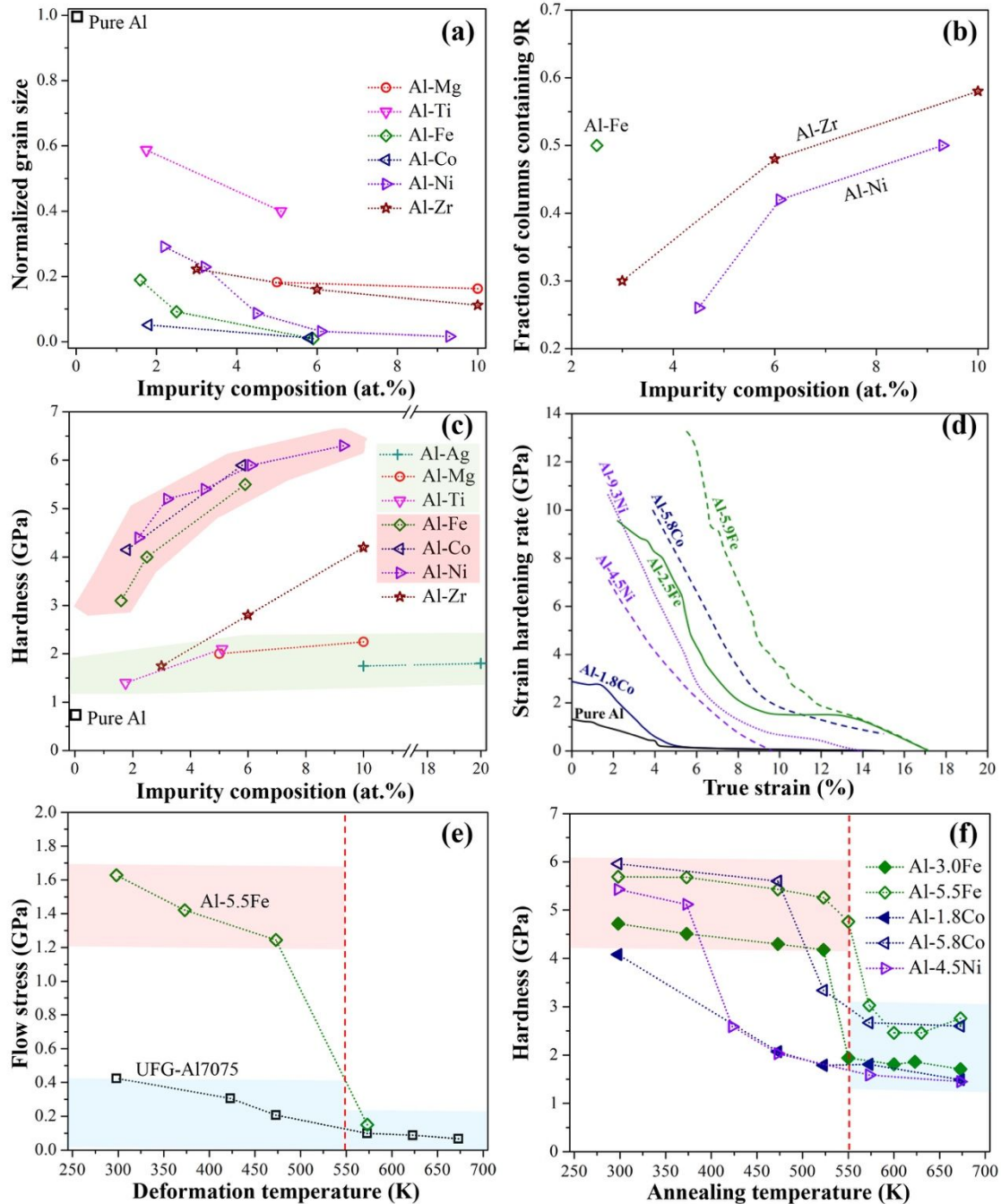


**Fig. 2** Summary of experimental data in sputtered Al-X alloys. (a) The influence of solutes on columnar grain size. (b) The fraction of columns containing 9R phase with solute concentration. (c) The hardness of as-deposited Al alloys with respect to solute concentration at room temperature. (d) The strain hardening rates derived from *in situ* micropillar compression tests at room temperature. (e) The flow stress of sputtered Al-Fe alloy and UFG-Al7075 micropillars at multiple temperatures. (f) The variation of hardness of Al-Fe, Al-Co and Al-Ni alloys with respect to annealing temperature.

Fig. 2(c) shows the indentation hardness of as-deposited Al-X alloy films with respect to solute concentration at room temperature. These Al alloy films have much higher hardness than pure Al film. Also, with similar solute concentration, Al-Fe, Al-Co and Al-Ni alloys have much higher hardness than Al-Mg, Al-Ti, Al-Zr and Al-Ag alloys. The nanoindentation data are comparable with the micro-pillar compression data. The hardness is nearly three times the flow stress (supplementary Fig. S1). Fig. 2(d) compares the strain hardening rates of pure Al, Al-Fe, Al-Co and Al-Ni pillars compressed at room temperature. For similar solute concentration and at the same strain level, Al-Fe alloys have higher hardening rates than Al-Co and Al-Ni alloys. The strain hardening in nanosized columns is mainly contributed by dislocation-GBs and dislocation-SFs/9R phases interactions. Thus, the highest strain hardening rate in Al-Fe alloys is consistent with its high volume fraction of 9R phases and the small columnar grain size, as shown in Fig. 2(b). More importantly, solutes enhance the thermal stability of Al-X alloys. As shown in Fig. 2(e), Al-Fe pillars exhibit much higher flow stress than ultra-fine grained (UFG) Al 7075 pillars when tested in the range of 298-473 K. Fig. 2(f) shows the hardness variation of Al-Fe, Al-Co and Al-Ni alloys with annealing temperatures. Compared to pure Al, Al-5.5Fe alloys (maintain high strength up to 553 K) have better thermal stability than Al-5.8Co (maintain high strength up to 473 K) and Al-4.5Ni alloys (maintain high strength up to 373 K). In addition, It is found that higher solute concentration results in better thermal stability.

### 3. Theoretical calculations

Experimental results clearly show that certain co-sputtering solutes can modify the microstructures and improve the thermal-mechanical properties of Al alloys. During deposition, one major factor affecting columnar grain size is diffusivity of adatoms. Fraction of 9R phase is related to the probability associated with formation and recovery of faulted surface clusters during deposition. Strengthening is contributed by solid solution strengthening, grain refinement and SFs. Ma *et al.*<sup>62</sup> estimated the solid solution strengthening with DFT calculations. For instance, 5.9 at.% Fe solutes cause  $\sim 0.15$  GPa increasement in critical resolved shear stress, which is far smaller than the measured high flow stress, 1.58 GPa. Therefore, strengthening in sputtered Al alloys is mainly contributed by grain refinement and SFs. The strain hardening is mainly caused by obstruction of dislocations. GBs, SFs/CTBs and 9R phases can be strong barriers for the movement of dislocations<sup>49, 63-65</sup>. Alloys with good thermal stability should maintain the super-saturation of solutes while prevent the motion of GBs. The activation energy of solute diffusion in bulk Al has

been calculated by Simonovic *et al.* <sup>66</sup>. Herein, first principles DFT calculations will be performed to reveal the effect of co-sputtering solutes on adatom diffusivity, energetics and kinetics of surface clusters, solute diffusivity in Al matrix and GB segregation.

**Table 1** Valence states of elements and k-mesh used during optimization of lattice parameters and cohesive energies, and optimized lattice parameters and cohesive energies.

Element	Valence	k-mesh	Structure	Lattice (Å)	Cohesive energy (eV)
Al	$3s^2 3p^1$	12×12×12	FCC	a=4.040	3.47
Mg	$3s^2$	19×19×11	HCP	a=3.189; c=5.194	1.52
Si	$3s^2 3p^2$	9×9×9	Diamond	a=5.469	4.54
Ti	$3p^6 3d^2 4s^2$	15×15×9	HCP	a=2.936; c=4.648	5.31
Fe	$3d^7 4s^1$	17×17×17	BCC	a=2.832	4.92
Co	$3d^8 4s^1$	19×19×13	HCP	a=2.491; c=4.025	5.17
Ni	$3d^8 4s^2$	13×13×13	FCC	a=3.518	5.08
Zn	$3d^{10} 4s^2$	19×19×11	HCP	a=2.637; c=5.072	1.11
Zr	$4s^2 4p^6 4d^2 5s^2$	15×15×9	HCP	a=3.232; c=5.169	6.45
Ru	$4d^7 5s^1$	19×19×11	HCP	a=2.713; c=4.281	7.97
Pd	$4d^9 5s^1$	12×12×12	FCC	a=3.942	3.79
Ag	$4d^{10} 5s^1$	12×12×12	FCC	a=4.146	2.53

Density function theory (DFT) calculations were conducted using the Vienna Ab initio Simulation Package (VASP) <sup>67, 68</sup>. The generalized gradient approximation (GGA) with Perdew-Burke-Ernzerhof (PBE) parametrization <sup>69</sup> is used for the exchange and correlation functions. The core electrons are replaced by the projector augmented wave (PAW) pseudopotentials <sup>70</sup> with the valence states shown in Table 1. A 500 eV cut-off on kinetic energy is used for the plane wave basis set. For all DFT calculations, the self-consistent iteration is stopped when the change of total energy is smaller than  $10^{-5}$  eV. The convergence criterion of geometry optimizations are that the forces acting on each atom is smaller than 0.01 eV/Å. Lattice parameters and cohesive energies are optimized for each element's thermodynamically stable structure at zero temperature and zero pressure. The models used are primitive cells. The associated Monkhorst-Pack (M-P) K-point grid <sup>71</sup> is summarized in Table 1. The calculated lattice parameters agree well with experiments <sup>72</sup> while cohesive energies is consistent with other DFT calculations <sup>73, 74</sup> and comparable to experimental results <sup>75</sup>. The details of models and setup of K-mesh associated with other calculations will be described later.

The microstructure of sputtered alloys is governed by the complex growth processes, involving adatom diffusivity <sup>76-78</sup>, cluster nucleation rate <sup>79-82</sup>, surface cluster diffusivity <sup>83, 84</sup>, grain boundary

mobility<sup>85-89</sup> and etc. The typical microstructure of sputtered Al and Al-X films is schematically shown in Fig. 1(b). These Al films have a sharp {111} texture due to the low surface energy of {111} surface<sup>90</sup>. Corresponding to the dominant {111} texture, the grain size is controlled by the diffusivities of adatom and clusters on {111} surface and the mobility of GBs. In each column, SFs and CTBs can be initiated from faulted surface clusters. The formation probability of faulted structures is related to the nucleation rate and recovery rate of faulted surface clusters, and both rates are determined by the formation energy and diffusivity of surface clusters<sup>79-84</sup>. For these columns sharing <111> tilt axis,  $\Sigma 3\{112\}$  ITBs with the lowest interface energy are energetically favorable<sup>61</sup>. Solute segregation<sup>91,92</sup> often occurs to ITBs with extra free volume<sup>93</sup>. In what follows, we performed DFT calculations to determine these physical quantities.

### 3.1 Modify adatom diffusivity on surface via co-sputtering solutes

Atomistic simulations<sup>76-78, 81, 83, 94-98</sup> and experiments<sup>79, 80, 82, 99-102</sup> have shown a high diffusivity of adatom and clusters on {111} surface due to low kinetic barrier. Presence of solutes can modify the kinetic barriers<sup>16,103</sup>, further tailoring grain size. The change of kinetic barriers by solute can be estimated, in the simplest fashion, by the extra energy needed to break neighboring bonds before diffusion<sup>103, 104</sup>. For example, first principles DFT calculations<sup>105</sup> showed that change of Ehrlich-Schwoebel (E-S) barrier associated with surface diffusion of a Cu adatom near a transition element solute shows a linear trend to the strength of Cu-solute bond. Therefore, we calculated the extra binding energy of an Al adatom on a flat {111} surface due to the presence of solute element via first principles DFT calculations. It should be noted the extra binding energy only reveals a trend but not the exact change in kinetic energy barrier. Fig. 3(a) shows two states that an Al adatom is close to and far from the solute on (111) surface, refer to as “close” and “far” states, respectively. Both states are represented by models with the dimension of  $9.91 \text{ \AA} \times 27.78 \text{ \AA} \times 11.44 \text{ \AA}$ . Both models contain a substrate composing four (111) atomic layers and an Al adatom. The lower three layers contain 48 Al atoms while the top layer contain 15 Al and 1 solute atoms. The solute atom locates at a substitution site. For the “close” state, the Al adatom (in dark red color) locates at a 1<sup>st</sup> nearest neighbor (NN) site of the solute (in grey color), and its binding to the substrate should be greatly affected by the solute. For the “far” state, the Al adatom (in red color) locates at a 6<sup>th</sup> NN site of the solute (in grey color), and is less affected by the solute. During relaxation, the bottom (111) layer (in blue color) is fixed. The first Brillouin zone was integrated

by  $6 \times 3 \times 6$  M-P K-points. By subtracting the system energy associated with “close” state from the system energy associated with “far” state, the extra binding energy for an Al adatom and a flat  $\{111\}$  surface due to the solute is calculated. Larger extra binding energy indicates lower adatom diffusivity near solutes.

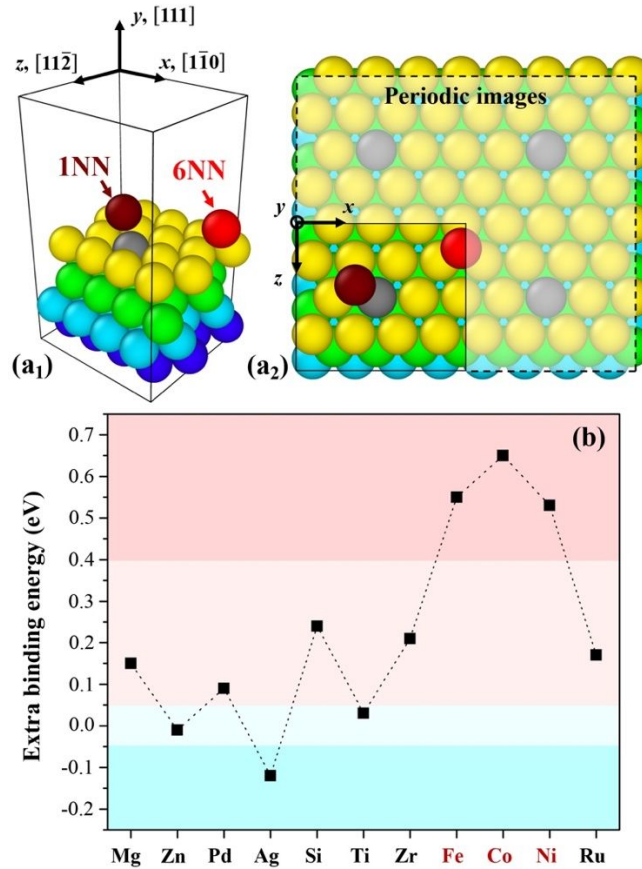


**Fig. 3** (a<sub>1</sub>) The atomic model for DFT calculations. Atoms are colored to show atomic layers. The gray atom represents the solute atom. The red and dark red atoms indicate two possible sites for adatoms. (a<sub>2</sub>) The top view of the model. A  $2 \times 2$  periodic image is used to illustrate the order of nearest neighbor sites. (b) Extra binding energy for an Al adatom due to one solute in the first atomic layer.

The extra binding energies associated with solute elements are shown in Fig. 3(b). In the figure, the sequence of elements follows number of unfilled electrons. Among 11 solute elements, Fe, Co and Ni solutes, which are next to each other on the same row of periodic table, provide the largest extra binding energy, suggesting obvious trapping effect on diffusion of Al adatoms. The extra binding energy associated with Mg, Si, Zr, Ru and Pd solutes is smaller than that associated with

Fe, Co and Ni solutes, indicating relatively weak trapping effect. The extra binding energy is nearly zero associated with solutes Ti and Zn and negative associated with Ag.

### 3.2 Modify SFE and energy barrier for the SF recovery via co-sputtering solutes

Solute atoms can modify the SFE of Al alloys<sup>62, 106</sup>. DFT calculations usually employed a slab model with one solute locating next to the SF and often ignored the statistical effect associated with possible distributions of solute atoms. For example, solute atoms may form solute pairs and triplets with first, second, third, and even fourth order neighboring bonds. Zhang *et al.*<sup>107</sup> showed that two Mg solutes in their 4<sup>th</sup> order NN positions have the lowest binding energy. Zhao *et al.*<sup>108</sup> proposed a bond breaking and forming model to calculate the SFEs in concentrated solid-solution alloys based on the distributions and types of bonds associated with local structure. Here, we estimated the SFE via DFT calculations based on the order and distributions of possible solute pairs in co-sputtered Al-X alloys.

Two sets of slab models as shown in Fig. 4(a<sub>1</sub>) (labeled as “perfect” model) and Fig. 4(a<sub>2</sub>) (labeled as “faulted” model) are employed. Each model contains 10 atomic layers, and each layer contains 16 atoms. The first Brillouin zone was integrated by  $5 \times 1 \times 5$  M-P K-points. The “faulted” model is obtained by shearing the “perfect” model with one of three partial vectors ( $1/6[11\bar{2}]$ ,  $1/6[1\bar{2}1]$  and  $1/6[\bar{2}11]$ ) across the shear plane (denoted by the short-dashed line). After the stacking sequence across a shear plane changes via gliding a partial dislocation, the numbers of different order neighboring bonds may vary, altering the solute-solute interaction energy and in turn modifying SFE and the energy barrier associated with the change of stacking sequence. Taking solute concentration of 6.25 at.% as an example, one Al atom in each (111) atomic layer is replaced by one solute. When one solute (grey) is placed in the lower layer next to the shear plane, another solute atom in the upper atomic layer next to the shear plane could locate at several positions labelled by black numbers for “perfect” model, as shown in Fig. 4(b<sub>1</sub>). Similarly, positions of the solute atom in the upper atomic layer are labelled by red numbers for “faulted” model, as shown in Fig. 4(b<sub>2</sub>). The solutes can be in each other’s 1<sup>st</sup>, 2<sup>nd</sup>, 3<sup>rd</sup>, 5<sup>th</sup> and 6<sup>th</sup> order NN positions. The “faulted” model can be achieved by shearing the “perfect” model with one of three partial dislocations ( $p_1$ ,  $p_2$  or  $p_3$ ). Fig. 4(b<sub>3</sub>)-(b<sub>5</sub>) show the three faulted structures with black number showing the original positions of atoms in lower atomic layer. By comparing Fig. 4(b<sub>2</sub>) and Fig. 4(b<sub>3</sub>)-(b<sub>5</sub>), we developed the relations  $p^{(ij)}$  to describe the probability of forming ( $j$ )<sup>th</sup>-NN “faulted”

pair from the “perfect” model containing ( $i$ )<sup>th</sup>-NN solute pair (Table 2). For example, for two solutes (grey atom and the atom enclosed by red circle) as each other’s 1<sup>st</sup> NN in the “perfect” model, shearing via  $\mathbf{p}_1$  and  $\mathbf{p}_2$  does not change the order of NN while shearing via  $\mathbf{p}_3$  causes 2<sup>nd</sup> NN. Thus,  $p^{(11)}$  is 0.66 while  $p^{(12)}$  is 0.33. We then conduct DFT calculations to relax the structures of “perfect” and “faulted” models. The top and bottom layers (in white color) are fixed to mimic bulk properties. Intrinsic stacking fault energy (ISFE) can be calculated based on the difference in system energies of the two states.

**Table 2** Relation between solute pairs in “perfect” and “faulted” models (with 6.25 at.% solute concentration). The probability refers to the chance that certain pair in “faulted” model can be achieved for given pair in “perfect” model.  $N$  is the number of possible solute pairs in perfect and “faulted” models.

Pair in “perfect” model	Pair in “faulted” model	Probability $p^{(ij)}$
1 <sup>st</sup> -NN, $N=3$	1 <sup>st</sup> -NN, $N=6$	$p^{(11)} = 0.66$
	2 <sup>nd</sup> -NN, $N=3$	$p^{(12)} = 0.33$
2 <sup>nd</sup> -NN, $N=3$	1 <sup>st</sup> -NN, $N=3$	$p^{(21)} = 0.33$
	3 <sup>rd</sup> -NN, $N=6$	$p^{(23)} = 0.66$
3 <sup>rd</sup> -NN, $N=6$	2 <sup>nd</sup> -NN, $N=6$	$p^{(32)} = 0.33$
	3 <sup>rd</sup> -NN, $N=6$	$p^{(33)} = 0.33$
	5 <sup>th</sup> -NN, $N=6$	$p^{(35)} = 0.33$
5 <sup>th</sup> -NN, $N=3$	3 <sup>rd</sup> -NN, $N=6$	$p^{(53)} = 0.66$
	6 <sup>th</sup> -NN, $N=3$	$p^{(56)} = 0.33$
6 <sup>th</sup> -NN, $N=1$	5 <sup>th</sup> -NN, $N=3$	$p^{(65)} = 1.00$

To statistically estimate the ISFE associated with a given solute pair in a “perfect” model, we introduced the probability of  $N$  possible solute pairs (as listed in Table 1) in “faulted” model and estimated the local ISFE by,

$$E_{ISF}^{(i)} = \left( \sum_j p^{(ij)} E_{faulted}^{(ij)} - E_{perfect}^{(i)} \right) / A \quad (1)$$

where  $E_{perfect}^{(i)}$  is the system energy of the “perfect” model containing one ( $i$ )<sup>th</sup>-NN solute pair,  $E_{faulted}^{(ij)}$  is the system energy of the “faulted” model containing one ( $j$ )<sup>th</sup>-NN solute pair,  $p^{(ij)}$  is the probability of forming ( $j$ )<sup>th</sup>-NN “faulted” pair from the “perfect” model containing ( $i$ )<sup>th</sup>-NN solute pair and  $A$  is area of the (111) layer.

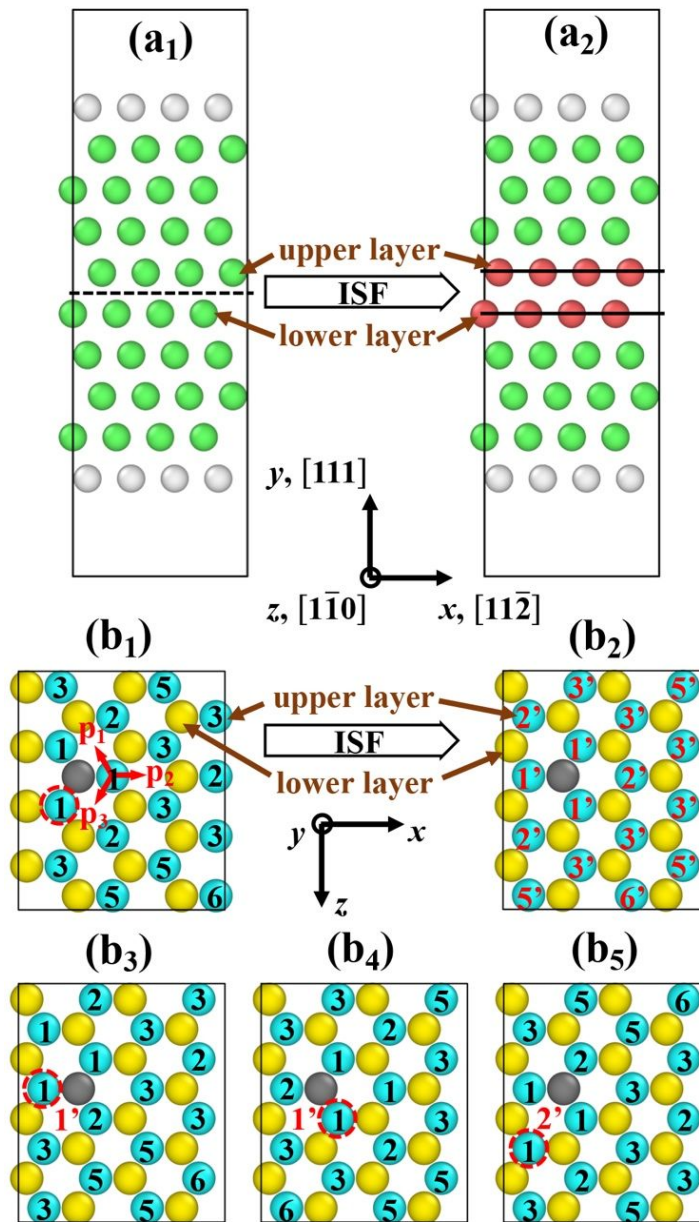


**Fig. 4** (a<sub>1</sub>) and (a<sub>2</sub>) Atomic models for perfect and faulted structures. (b<sub>1</sub>) Two adjacent atomic layers in a “perfect” structure showing the possible solute pairs and (b<sub>2</sub>) Two adjacent atomic layers in a “faulted” structure showing the possible solute pairs. Illustrations for the change in solute pairs associated with shearing the perfect model containing 1-NN solute pair with (b<sub>3</sub>)  $p_1$ , (b<sub>4</sub>)  $p_2$  and (b<sub>5</sub>)  $p_3$ .

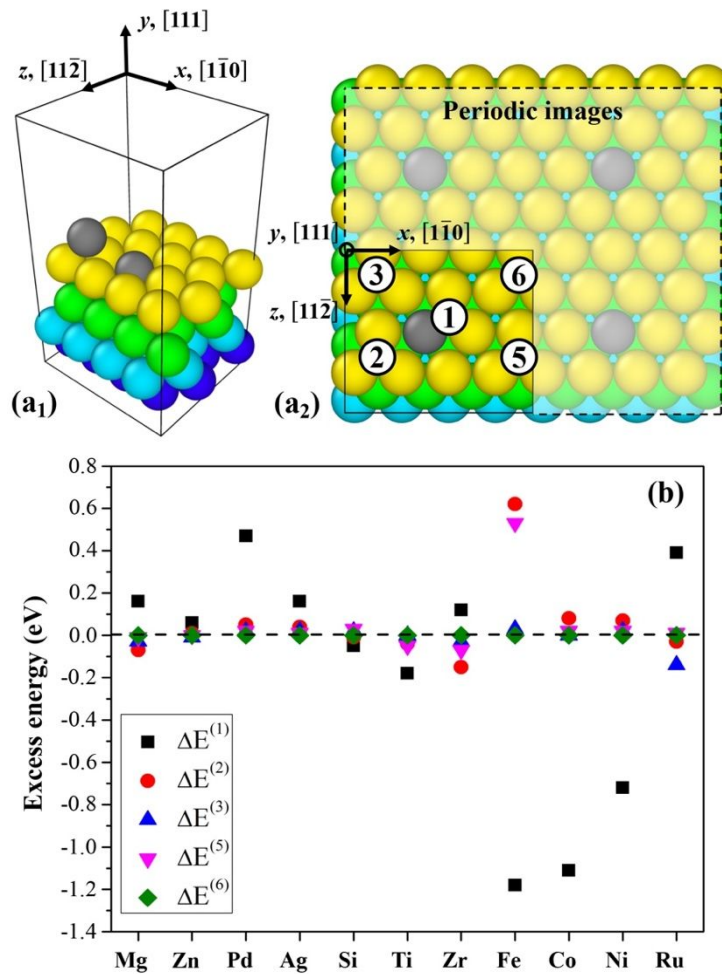


**Fig. 5** (a) The atomic model for DFT calculations. Atoms are colored to show atomic layers. The gray atom represents the solute atom. (b) The top view of the model. A  $2 \times 2$  periodic image is used to illustrate the order of NN sites. (c) The excess energies for 1<sup>st</sup>, 2<sup>nd</sup>, 3<sup>rd</sup>, 5<sup>th</sup> and 6<sup>th</sup> order NN pairs.

Considering the probabilities  $P^{(i)}$  of forming possible ( $i$ )<sup>th</sup>-NN “perfect” models, the average ISFE ( $E_{ISF}$ ) is estimated by,

$$E_{ISF} = \sum_i P^{(i)} E_{ISF}^{(i)} \quad (2)$$

The probability of forming the ( $i$ )<sup>th</sup>-NN “perfect” model  $P^{(i)}$  is determined based on the energetics of solute pairs on surface during deposition. The model shown in Fig. 5(a<sub>1</sub>) has the dimension of  $9.91 \text{ \AA} \times 27.78 \text{ \AA} \times 11.44 \text{ \AA}$ , and contains four (111) atomic layers and a solute adatom. Each (111) atomic layer contains 16 atoms. The top layer contains 15 Al and 1 solute atoms. Fig. 5(a<sub>2</sub>) indicates the possible sites for the solute atom, denoted by the 1<sup>st</sup>, 2<sup>nd</sup>, 3<sup>rd</sup>, 5<sup>th</sup> and 6<sup>th</sup> order NN sites. The first Brillouin zone was integrated by  $6 \times 3 \times 6$  M-P K points for the DFT

calculation. Two solutes in their 6<sup>th</sup> order NN positions are treated as two isolated solutes and the corresponding system energy is used as reference. The excess energies  $\Delta E^{(1)}$ ,  $\Delta E^{(2)}$ ,  $\Delta E^{(3)}$ ,  $\Delta E^{(5)}$  and  $\Delta E^{(6)}$  for 1<sup>st</sup>, 2<sup>nd</sup>, 3<sup>rd</sup>, 5<sup>th</sup> and 6<sup>th</sup> order NN pairs are plotted in Fig. 5(b). The probability of (*i*)<sup>th</sup>-NN “perfect” model  $P^{(i)}$  is estimated following the Arrhenius relation that,

$$P^{(i)} = \exp\left(-\frac{\Delta E^{(i)}}{k_B T}\right) / \sum_j \exp\left(-\frac{\Delta E^{(j)}}{k_B T}\right) \quad (3)$$

$k_B$  is the Boltzmann constant.

**Table 3** Values of  $\Delta E^{(i)}$  and estimation of  $P^{(i)}$  at 300 K for different solutes for cases with 6.25 at.% solute concentration.

Element	1 <sup>st</sup> NN		2 <sup>nd</sup> NN		3 <sup>rd</sup> NN		5 <sup>th</sup> NN		6 <sup>th</sup> NN	
	$\Delta E^{(1)}$	$P^{(1)}$	$\Delta E^{(2)}$	$P^{(2)}$	$\Delta E^{(3)}$	$P^{(3)}$	$\Delta E^{(5)}$	$P^{(5)}$	$\Delta E^{(6)}$	$P^{(6)}$
<b>Mg</b>	0.16	0.00	-0.07	0.74	-0.03	0.13	-0.01	0.08	0	0.05
<b>Si</b>	-0.05	0.68	-0.01	0.15	0.02	0.05	0.03	0.03	0	0.10
<b>Ti</b>	-0.18	0.98	-0.04	0.01	0.00	0.00	-0.05	0.01	0	0.00
<b>Fe</b>	-1.18	1.00	0.62	0.00	0.03	0.00	0.53	0.00	0	0.00
<b>Co</b>	-1.11	1.00	0.08	0.00	0.00	0.00	0.02	0.00	0	0.00
<b>Ni</b>	-0.72	1.00	0.07	0.00	0.02	0.00	0.02	0.00	0	0.00
<b>Zn</b>	0.06	0.03	0.01	0.16	-0.01	0.35	0.00	0.21	0	0.24
<b>Zr</b>	0.12	0.00	-0.15	0.96	-0.03	0.01	-0.07	0.03	0	0.00
<b>Ru</b>	0.39	0.00	-0.03	0.01	-0.14	0.98	0.01	0.00	0	0.00
<b>Pd</b>	0.47	0.00	0.05	0.06	0.02	0.22	0.02	0.23	0	0.48
<b>Ag</b>	0.16	0.00	0.04	0.10	0.02	0.20	0.01	0.29	0	0.41

Here, we take the Al-6.25Fe system as an example to show the estimation of average SFEs, and compare the results of Al-6.25Fe and pure Al. The system energies of “perfect” models with 1<sup>st</sup>, 2<sup>nd</sup>, 3<sup>rd</sup>, 5<sup>th</sup> and 6<sup>th</sup> order NN pairs are -597.59, -597.60, -597.56, -597.63 and -597.51 eV. The system energies of “faulted” models with 1<sup>st</sup>, 2<sup>nd</sup>, 3<sup>rd</sup>, 5<sup>th</sup> and 6<sup>th</sup> order NN pairs are -596.64, -596.55, -596.50, -596.57 and -596.50 eV. With area  $A$  equal to 113.37 Å<sup>2</sup>, the local ISFEs  $E_{ISF}^{(1)}$ ,  $E_{ISF}^{(2)}$ ,  $E_{ISF}^{(3)}$ ,  $E_{ISF}^{(5)}$  and  $E_{ISF}^{(6)}$  are estimated with Eq. (1) to be 139.10, 148.24, 143.78, 159.18 and 133.64 mJ/m<sup>2</sup>. Table 3 summarizes the values of  $\Delta E^{(i)}$  and  $P^{(i)}$  for different solute pairs at room temperature. The “perfect” model with 1<sup>st</sup> NN pair should be dominant since  $P^{(1)}$  is nearly one. Following Eq. (2), the average ISFE is 139.10 mJ/m<sup>2</sup>.

**Table 4** Possibility  $p^{(ij)}$  between solutes pairs in “perfect” and “faulted” models with 12.5 at.% solute concentration.

$p^{(11)} = 0.66$	$p^{(21)} = 0.50$	$p^{(32)} = 0.33$
$p^{(12)} = 0.33$	$p^{(23)} = 0.50$	$p^{(31)} = 0.66$

**Table 5** Values of  $\Delta E^{(i)}$  and estimation of  $P^{(i)}$  at 300 K for different solutes for cases with 12.5 at.% solute concentration.

Element	1 <sup>st</sup> NN		2 <sup>nd</sup> NN		3 <sup>rd</sup> NN	
	$\Delta E^{(1)}$	$P^{(1)}$	$\Delta E^{(2)}$	$P^{(2)}$	$\Delta E^{(3)}$	$P^{(3)}$
<b>Mg</b>	0.16	0.00	-0.07	0.85	-0.03	0.15
<b>Si</b>	-0.05	0.78	-0.01	0.17	0.02	0.05
<b>Ti</b>	-0.18	0.99	-0.04	0.01	0.00	0.00
<b>Fe</b>	-1.18	1.00	0.62	0.00	0.03	0.00
<b>Co</b>	-1.11	1.00	0.08	0.00	0.00	0.00
<b>Ni</b>	-0.72	1.00	0.07	0.00	0.02	0.00
<b>Zn</b>	0.06	0.05	0.01	0.30	-0.01	0.65
<b>Zr</b>	0.12	0.00	-0.15	0.99	-0.03	0.01
<b>Ru</b>	0.39	0.00	-0.03	0.01	-0.14	0.99
<b>Pd</b>	0.47	0.00	0.05	0.22	0.02	0.78
<b>Ag</b>	0.16	0.00	0.04	0.34	0.02	0.66

To reveal the effect of solute concentration on ISFE, we also calculated the average ISFE for different solute elements with solute concentration of 12.5%. Two sets of slab models are employed. Each model contains 10 (111) atomic layers, and each layer contains 8 atoms. The first Brillouin zone was integrated by  $3 \times 1 \times 5$  M-P K-points. The “faulted” model is obtained by shearing the “perfect” model with one of three partial vectors ( $1/6[11\bar{2}]$ ,  $1/6[1\bar{2}1]$  and  $1/6[\bar{2}11]$ ) across the shear plane (denoted by the short-dashed line). For solute concentration of 12.5 at.%, one Al atom in each (111) atomic layer is replaced by one solute. Two solutes on two layers next to shear plane can be in each other’s 1<sup>st</sup>, 2<sup>nd</sup> and 3<sup>rd</sup> order positions. Considering the change in stacking sequence via shearing the “perfect” model with one of three partial vectors, we developed the relations  $p^{(ij)}$  as summarized in Table 4. Using the same method, the values of  $\Delta E^{(i)}$  and  $P^{(i)}$  for different solute pairs at room temperature are calculated and summarized in Table 5. Then, all possible “perfect” and “faulted” models are relaxed, and the average ISFE was estimated according to Eq.(2).

The average ISFE were plotted in Fig. 6(a). For Al-6.5X system, these solutes do not significantly modify the ISFE. The maximum decrease of the ISFE is 20.64 mJ/m<sup>2</sup> for the Al-6.25Ti system, and the maximum increase of the ISFE is 6.64 mJ/m<sup>2</sup> for the Al-6.5Pd systems. When the solute concentration is increased up to 12.5%, the change in the ISFE is obvious. But the maximum decrease is about 54.18 mJ/m<sup>2</sup> for the Al-12.5Ti system. Even so, the ISFE is still too high to form and stabilize SFs. Therefore, the formation and stabilization of SFs during deposition should be kinetically facilitated.

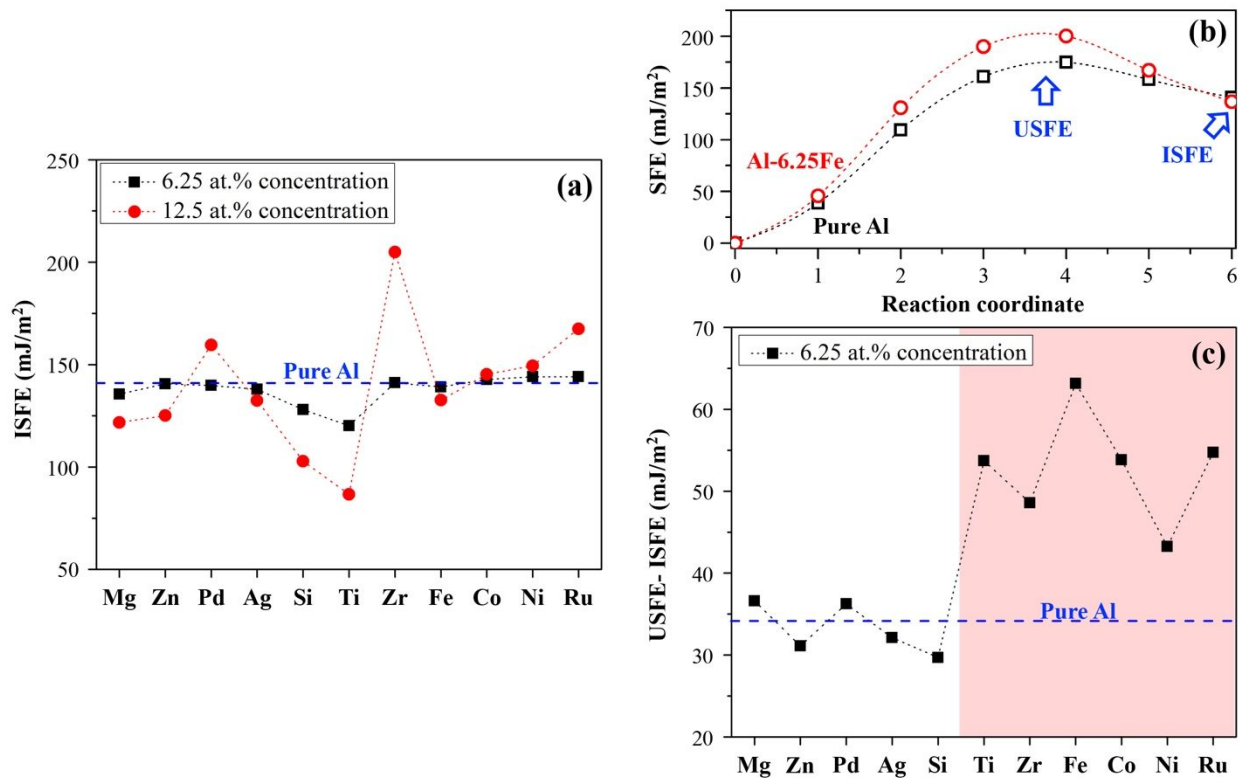


**Fig. 6** (a) ISFE in sputtered Al alloys with 6.25 at.% and 12.5 at.% solute concentration. (b) Variation of generalized SFE in pure Al and Al-6.25Fe on (111) plane. (c) ISF recovery barrier (USFE – ISFE) in sputtered Al alloys with 6.25 at.% solute concentration.

To understand the kinetically-facilitated formation of SFs, we further calculated the energy profile associated with the transition between the perfect and faulted structures. For a pair of “perfect” and “faulted” structures, a chain of five transient states (labeled as “state- $k$ ”,  $k = 1, 2, \dots, 5$ ) is produced by linearly interpolating between them. The intermediate state models are relaxed while fixing the movement of atoms on the (111) planes. The SFE associated with “state- $k$ ” is calculated based on the difference in system energies between “state- $k$ ” and “perfect” models with

similar forms of Eq. (1) and (2). Fig. 6(b) shows the generalized SFEs in pure Al (black curve) and Al-6.25Fe (red curve). The ISFEs of pure Al (140.85 mJ/m<sup>2</sup>) and Al-6.25Fe (139.10 mJ/m<sup>2</sup>) are close, but the unstable stacking fault energy (USFE) of Al-6.25Fe (199.94 mJ/m<sup>2</sup>) is higher than that of pure Al (174.80 mJ/m<sup>2</sup>). Consequently, the energy barrier associated with the ISF recovery (which is the difference between USFE and ISFE) of Al-6.25Fe (60.84 mJ/m<sup>2</sup>) is higher than that of pure Al (33.95 mJ/m<sup>2</sup>). Using the same method, we calculated the SFE profiles associated with different solute elements.

Fig. 6(c) shows the variation of the energy barrier for ISF recovery with solute element. It is found that Mg, Si, Zn, Pd and Ag solutes do not significantly modify the energy barrier for ISF recovery. Meanwhile, Ti, Fe, Co, Ni, Zr and Ru solutes can increase the energy barrier for ISF recovery to some extent. Among them, Fe solutes have the most significant effect.

### 3.3 Modify energetics and kinetics of surface clusters via co-sputtering solutes

A surface cluster is mobile if the time needed to move ( $\tau_{\text{cluster}}$ ) is smaller than the time needed to add an additional atom ( $\tau_{+1}$ ), and is immobile if not. Consequently, high deposition flux that reduces  $\tau_{+1}$  and low deposition temperature that increases  $\tau_{\text{cluster}}$  could stabilize surface clusters. If critical sizes of immobile perfect and faulted surface clusters are  $(i + 1)$  and  $(j + 1)$  atoms, the fraction of the mobile  $i$ -atoms perfect surface clusters over mobile  $j$ -atoms faulted surface clusters follows the Boltzmann distribution. So, the distribution of immobile surface clusters reflects the equilibrium distribution of the mobile  $i$ -atoms perfect and  $j$ -atoms faulted surface clusters. Immobile faulted surface clusters further develop into SFs and CTBs. Therefore, large fraction of SFs and CTBs are resulted from the small energy difference between  $i$ -atom perfect and  $j$ -atom faulted surface clusters, which requires low energy of faulted stacking of surface cluster or small difference between number  $i$  and  $j$ . For a given deposition temperature and flux, the value of  $i$  and  $j$  is related to kinetic barriers of perfect and faulted surface clusters. Thus, the probability of forming faulted islands increases with decreasing the energy of faulted stacking of surface clusters and increasing the kinetic barrier for the recovery of faulted surface clusters<sup>109, 110</sup>.

We investigate energetics and kinetics of surface trimer (three atoms) and surface heptamer (seven atoms). For a trimer, there are two types of perfect structures and two types of faulted structures. The type-H and the type-T perfect/faulted trimers have the centers on an HCP site and an top site. Type-H perfect and faulted trimers are more energetically favored than type-T perfect

and faulted trimers<sup>83</sup>. The recovery of faulted trimers can be achieved by concerted translation, concerted rotation and transformation between compact and linear trimers<sup>83, 84, 111</sup>. A type-H faulted trimer or a type-T faulted trimer can recover to a type-T perfect trimer or a type-H perfect trimer by the concerted translation as indicated by the arrows in Fig. 7(a<sub>1</sub>) and (a<sub>2</sub>). For a heptamer, there are one perfect and faulted structures, and they can be related by the concerted translation denoted by the arrows as shown in Fig. 7(a<sub>3</sub>)<sup>112</sup>. The energetic and kinetics of surface trimers and heptamers are calculated with the models shown in Fig. 7(a<sub>1</sub>)-(a<sub>3</sub>) that are composed of the 4-layer substrate (64 atoms) and a surface cluster. Al adatoms are colored in red and solute adatom is colored in grey. We first conducted energy minimization for the faulted structures and the recovered structures with the bottom 16 atoms fixed and the first Brillouin zone integrated by 6×3×6 M-P K-points. Then, a chain of transient states is produced by linearly interpolating between the recovered and faulted structures. It should be noted that a perfect linear translation may not be associated with the minimum energy path<sup>111</sup>. However, the employment of linear translation is much more computationally efficient and able to reveal the trend of solutes' effect on diffusivity of surface clusters.

Here, we take the Al-Fe system as an example. Fig. 7(b<sub>1</sub>) and (b<sub>2</sub>) shows the variation of the excess energy associated with the transition between a perfect trimer and the corresponding faulted trimer in pure Al and Al-Fe system. For pure Al, a type-H perfect trimer has the lowest formation energy and is used as reference to calculate the excess energy of other structures. Type-T perfect trimer, type-H faulted trimer and type-T faulted trimer have the excess energies of 0.04, 0.05 and 0.09 eV. The trend that type-H perfect/faulted trimers are energetically favorable than type-T perfect/faulted trimers is consistent with previous DFT works<sup>84</sup>. The slight difference in exact values is caused by the different selection of exchange and correlation functions (GGA in this work while LDA in ref<sup>84</sup>). When the cluster contains one Fe solute, the excess energies of type-T perfect trimer, type-H faulted trimer and type-T faulted trimer are 0.13, -0.05 and 0.11 eV. Fe solute effectively reduces the excess energy of type-H faulted trimer. The addition of solute may also modify the kinetic barrier associated with diffusion of surface trimers. In pure Al, the barrier associated with concerted translation from type-H perfect trimer to type-T faulted trimer (inverse of path 1 in Fig. 7(a<sub>1</sub>)) is 0.36 eV, which is higher than the barrier (0.33 eV) associated with concerted translation from type-H faulted trimer to type-T perfect trimer (path 2 in Fig. 7(a<sub>2</sub>)). The difference between two barriers is 0.03 eV. In comparison, with one Fe solute, the kinetic barriers

associated with inverse of path 1 and path 2 are 0.43 and 0.45 eV, resulting a -0.02 eV difference. In other words, presence of Fe solute makes diffusion of all types of trimers hard. Recovery of type-H faulted trimers is more difficult than faulting of type-H perfect trimers. As shown in Fig. 7(b<sub>3</sub>), the excess energy of a faulted heptamer is 0.32 eV with respect to a perfect heptamer in pure Al. The kinetic barrier associated with recovery of a faulted heptamer is 0.32 eV. When the cluster contains on Fe solute, the excess energy of a faulted heptamer is reduced to 0.22 eV, but the kinetic barrier associated with recovery of a faulted heptamer is increased to 0.73 eV, suggesting easier formation and harder recovery of faulted heptamers. In a brief, addition of Fe solute effectively reduces the formation energy of faulted surface clusters while increases the kinetic barrier associated with the recovery of faulted surface clusters, thus promoting the probability of growing faulted islands and facilitating formation of SFs/CTBs.

Using the same method, we calculated the energetics and kinetics of surface clusters with respect to solute element. The variation of excess energies of type-H faulted trimer with respect to type-H perfect trimer and faulted heptamer with respect to perfect heptamer with solute element is shown in Fig. 7(c<sub>1</sub>). The black and red dashed lines show the excess energies of type-H faulted trimer (0.05 eV) and faulted heptamer (0.32 eV) in pure Al. Except Si solute, all solutes reduce the excess energy of faulted surface clusters. In general, the excess energy is larger when a surface cluster contains more atoms, indicating easier formation of faulted stackings at low deposition temperature and with large deposition flux. It is found that the excess energy of type-H faulted trimer with one Mg, Fe, Ni, Zn, Ru, Pd or Ag is negative, suggesting that the formation of faulted trimers in these systems is energetically favorable. Meanwhile, all faulted heptamers have positive excess energy. The effect of Ti, Fe, Co, Zr and Ru solutes on reduction of excess energy of faulted heptamer is extraordinary. The reduction is ~45% for Ru solute. It should be noted that Ti and Zr, Fe and Ru are in the same group in periodic table, thus having similar effect. The variation of recovery barrier of type-H faulted trimer and faulted heptamer is shown in Fig. 7(c<sub>2</sub>). The black and red dashed lines show the recovery barrier of type-H faulted trimer (0.33 eV) and faulted heptamer (0.32 eV) in pure Al. Larger faulted surface cluster does not guarantee better stability. Addition of Ti, Fe, Co, Ni, Zr, Ru and Pd solutes effectively increase the recovery barrier. Faulted surface clusters containing those solutes are very stable once they form. It should be noted that the effect of Fe and Ru solutes on increasing the recovery barrier is the most exceptional.

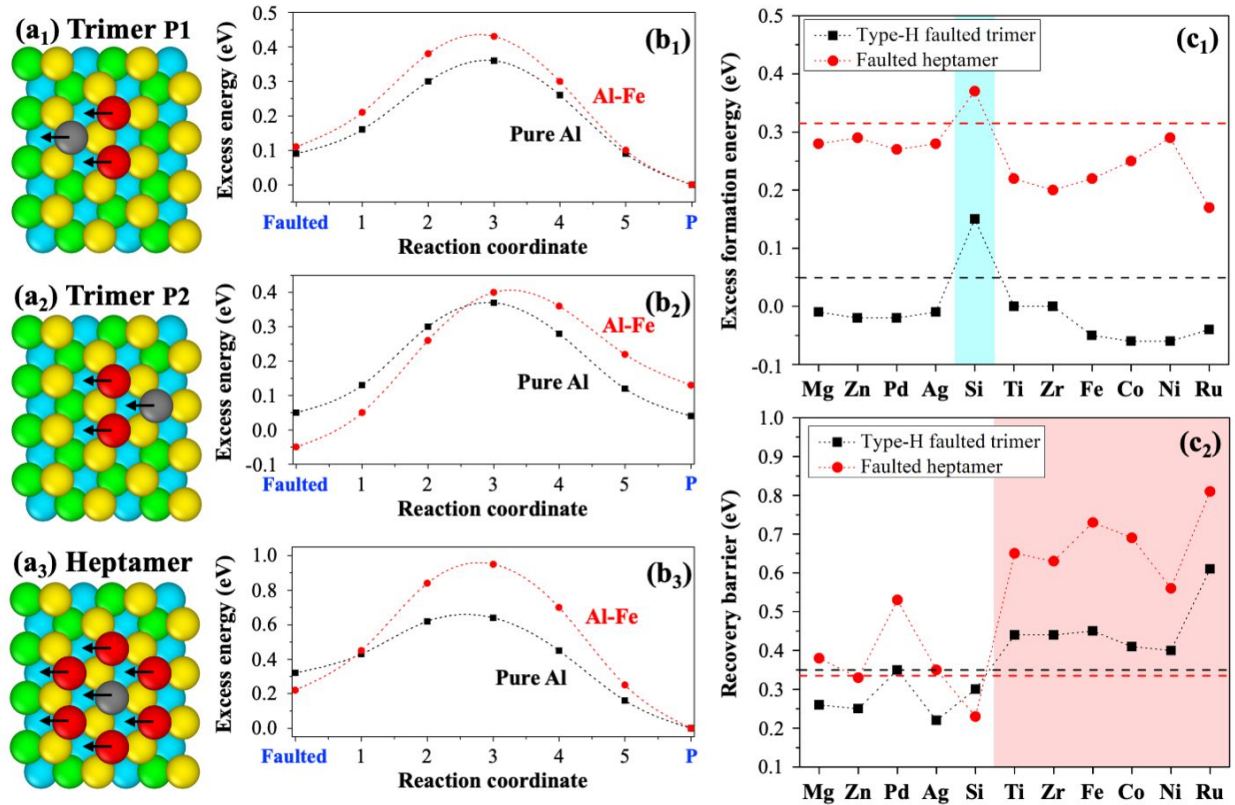


**Fig. 7** Models used for DFT calculations of energetics and kinetics of faulted surface clusters. (a<sub>1</sub>) Path 1 associated with recovery from type-T faulted trimer to type-H perfect trimer. (a<sub>2</sub>) Path 2 associated with recovery from type-H faulted trimer to type-T perfect trimer. (a<sub>3</sub>) Path 3 associated with recovery from faulted heptamer to perfect heptamer. (Al adatoms are colored in red and solute adatom is colored in grey.) Energy profiles associated with (b<sub>1</sub>) path 1, (b<sub>2</sub>) path 2 and (b<sub>3</sub>) path 3 in pure Al and Al-Fe system. (c<sub>1</sub>) Excess formation energy of type-H faulted trimer with respect to type-H perfect trimer and faulted heptamer with respect to perfect heptamer. (c<sub>2</sub>) Energy barrier associated with recovery of type-H faulted trimer and faulted heptamer.

### 3.4 Solute segregation at ITBs

For *nt* Al-X alloys, grain coarsening is accomplished by migration of ITBs. ITB can be treated as an array of partial dislocations with total Burgers content equal/nearly zero. ITB migration can be resulted from dislocation-ITB interaction<sup>44</sup>, or nucleation and glide of discrete partial dislocations<sup>113</sup>, or collective glide of partial dislocations<sup>113</sup>. Disregarding the difference among these phenomena, the migration of ITB is accomplished via glide of partial dislocations through the start-stop-start mechanism<sup>113</sup> accompanied with the dissociation of a condensed pileup of partial dislocations. Lower ISFE will promote the dissociation of the ITB and facilitate its

migration. Solute segregation at ITBs may retard or speed up the migration of ITBs because of the competition between solute pinning and solute reduced ISFE. Therefore, stable ITBs require high ISFE and strong solute segregation.

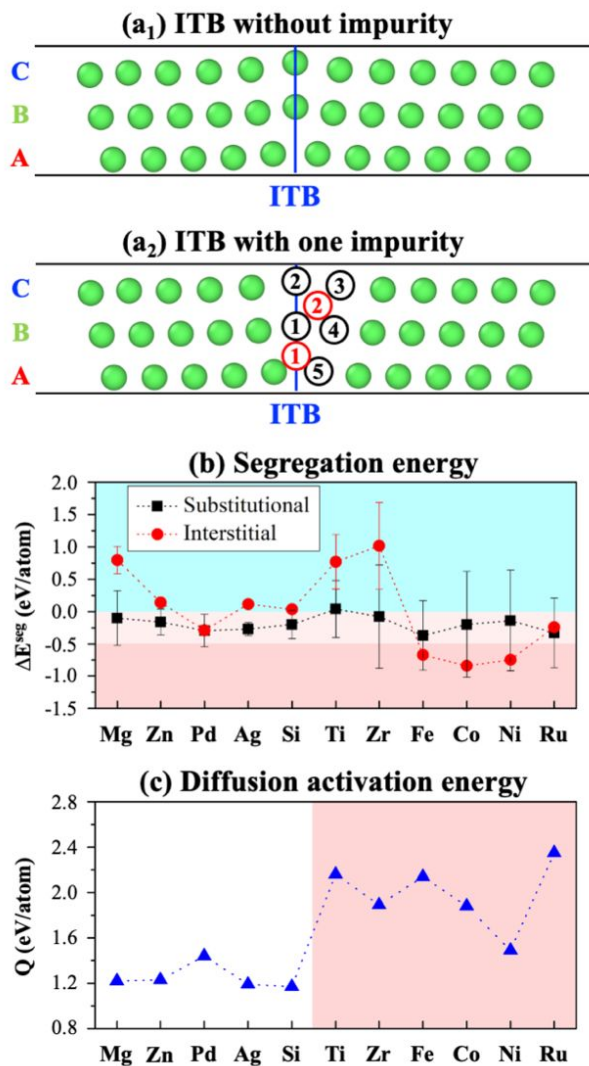


**Fig. 8** Atomic models with ITBs containing (a<sub>1</sub>) 105 Al atoms (a<sub>2</sub>) 105 Al atoms and 1 interstitial solute atom (possible sites for interstitial solute are labelled by red numbers in circles) or 104 Al atoms and 1 substitutional solute atom (possible sites for interstitial solute are labelled by black numbers in circles). (b) Variation of segregation energy at ITBs with solute. (c) Diffusion activation energy for solute in FCC Al.

The segregation energy is computed with slab models with one ITB as shown in Fig. 8(a<sub>1</sub>) and (a<sub>2</sub>). The model in Fig. 8(a<sub>1</sub>) contains 105 Al atoms. The model in Fig. 8(a<sub>2</sub>) contains 105 Al atoms and 1 interstitial solute atom or 104 Al atoms and 1 substitutional solute atom. In Fig. 8(a<sub>2</sub>), five possible substitutional sites and two possible interstitial sites are labelled by black and red numbers

in circles. With the first Brillouin zone integrated by  $4 \times 1 \times 4$  M-P K-points, the system energies of the two models are calculated and formation energy of substitutional/interstitial solute is estimated as  $E_s^{(ITB)}$ . The segregation energy is estimated by  $E_s^{(ITB)} - E_s^{(bulk)}$ , where  $E_s^{(bulk)}$  is the formation energy of a substitution in bulk Al. More negative segregation energy suggests stronger segregation. The segregation energy with respect to type of solute element is shown in Fig. 8(b). All studied elements could produce negative segregation energy, indicating that ITBs are energetically preferred sites for solutes. Binary alloys with segregation energy  $\leq -0.5$  eV/atom are regarded as strongly segregating system<sup>114</sup>. In this sense, Fe, Co and Ni interstitials can strongly segregate at ITBs. Owing to the negative segregation energy, high concentration of solute at/near ITBs is expected. Consequently, the ISFE near ITBs could be different from that in the grain interior. Fig. 6(b) shows the ISFE with different solute elements when solute concentration is 6.25 at.% and 12.5 at.%. It is found that higher concentration of Mg, Si and Ti solutes induces lower ISFE. Meanwhile, higher concentration of Zr, Ru and Pd solutes induces larger ISFE.

It is noted that the co-sputtered Al-X alloys have much higher solute concentration than the equilibrium solubility<sup>115</sup>, but secondary phases do not form during deposition<sup>46,49-51</sup>. In principle, second phases may form when the sputtered Al alloys are annealed at high temperatures. To remain the as-deposited microstructures, a high activation energy for solute diffusion is desired. The activation energy of solute diffusion in Al has been calculated by Simonovic *et al.*<sup>66</sup> via first principles calculations. Fig. 8(c) shows the variation of solute diffusion activation energy with solute elements. It is found that the diffusion activation energy of Ti, Fe, Co, Zr and Ru solutes are large. Among them, Fe and Ru solutes are the hardest to diffuse.

## 4. Discussion

### 4.1 Strengthen Al-xm alloys via refining grain size

A large extra binding energy between Al adatom and  $\{111\}$  surface due to solutes is likely to increase kinetic barrier associated with surface diffusion of adatoms. Fig. 3(b) shows the variation of extra binding energy with solute elements. It is expected that addition of Fe, Co and Ni solutes with large extra binding energy may significantly reduce grain size, addition of Mg, Si, Zr, Ru and Pd solutes with moderate extra binding energy may have relatively weak effect on grain refinement, while addition of Ti, Zn and Ag solutes with nearly zero or negative extra binding energy may have negligible effect on grain refinement. The statistical analysis from experiments in Fig. 2(a) is

consistent with the prediction based on the argument of extra binding energy. Ag solute results in negative extra binding energy, facilitating diffusion of Al adatoms and resulting a large grain size. For the other Al-X alloys, in general, higher solute concentration results in smaller grain size. Especially, Fe, Co and Ni solutes significantly refine grain size. Even for a relatively low concentration ( $\sim 2$  at.%), the columnar grain size in Al-1.6Fe, Al-1.8Co and Al-2.2Ni alloys is significantly reduced about 81%, 95% and 71% of the columnar grain size in sputtered pure Al. A high concentration ( $>6$  at.%) leads to more than 95% reduction of columnar grain size. Mg and Zr solutes have moderate effect on grain refinement. For example, the reduction of grain size in Al-5.0Mg and Al-6.0Zr alloys is 78% and 84%. Grain size reduction in Al-5.1Ti alloy is 60%, indicating relatively weak effect of Ti solute on grain refinement.

Accompanied with refining grain size, co-sputtered Al-X alloys exhibit improved strength. Addition of Fe, Co and Ni solutes significantly improves strength of Al-X alloys. For example, a relatively low concentration ( $\sim 2$  at.%) results in large enhancement in hardness (3.1 GPa, 4.2 GPa and 4.4 GPa for Al-1.6Fe, Al-1.8Co and Al-2.2Ni alloys). An increase in concentration obviously enhance the hardness. Al-X alloys with high concentration ( $>6$  at.%) of Fe, Co and Ni solutes have hardness more than 5.5 GPa. In comparison, the hardness of Al-5.0Mg, Al-5.1Ti and Al-6.0Zr is 2.0, 2.1 and 2.8 GPa, respectively, indicating a weak strengthening effect. This is partially attributed to the large columnar grain size due to the small extra binding energy associated with solutes Mg, Ti and Zr. It should be noted that grain size is not the only factor affecting the strength of co-sputtered Al-X alloys. The density of SFs and 9R phase bands in each column is another factor besides solid solution hardening.

#### **4.2 Formation of SFs and 9R phase and strain hardening behavior**

DFT calculations revealed that metal solutes reduce the energy difference between faulted and perfect surface clusters and increase the energy barriers associated with recovery of faulted surface clusters, promoting formation of SFs and kinetically stabilizing the formed SFs. SFs are strong barriers to dislocation motion and greatly contribute to strengthening and strain hardening<sup>49, 63-65</sup>. In experiments, statistics of 9R phase (Fig. 2(b)) indicates that Fe solute is more effective in promoting formation of SFs than Zr and Ni solutes. The black curve in Fig. 6(a) shows the variation of ISFE with solute elements when solute concentration is 6.25 at.%. It is found that these solutes do not significantly modify the ISFE, implying that the formation of SFs during deposition should

be kinetically facilitated. As shown in Fig. 7(c<sub>1</sub>) and (c<sub>2</sub>), among Fe, Ni and Zr solutes, Fe solutes have the most significant effect on reducing the excess energy and increasing the energy barrier for the recovery of faulted surface clusters. For surface cluster containing a Zr or Ni solute, type-H faulted trimer with one Ni solute has lower excess energy and faulted heptamer with one Zr solute has lower excess energy. Meanwhile, both faulted trimer and heptamer with Zr solutes have higher recovery barrier than faulted trimer and heptamer with Ni solutes. The DFT results reasonably account for the statistics of 9R phase (Fig. 2(b)) in Al-Fe, Al-Ni and Al-Zr alloys. High density of SFs generally results in high strain hardening rate. For example, DFT results show that Fe solute induces smaller excess energy and higher recovery barrier than Co solute and Ni solute. This indicates that Al-Fe alloys have higher density of SFs and strain hardening rate than Al-Co alloys and Al-Ni alloys, which agrees well with experimental results shown in Fig. 2(d). Based on DFT results, Ru solute is another candidate that can significantly promote formation of SFs.

### 4.3 Enhance thermal and mechanical stability of microstructures

During loading, SFs may annihilate via glide of Shockley partial dislocation while fine columnar grains may coarsen via migration of ITBs. Such processes can be facilitated by high temperature. It is reasonably believed that higher recovery barrier for faults will stabilize faulted structures and retard the annihilation. The recovery barrier is defined as the difference between USFE and ISFE. Fig. 6(c) shows the variation of ISF recovery barrier with solute element when solute concentration is 6.25 at.%. It is found that Mg, Si, Zn, Pd and Ag solutes do not modify the recovery barrier. Meanwhile, Ti, Fe, Co, Ni, Zr and Ru solutes increase the recovery barrier. Among them, the effect of Fe solute on increasing recovery barrier is the most remarkable. However, the recovery barrier in Al-Fe system is still much smaller than the recovery barrier in pure Ni or Cu. Based on first principles DFT calculations, we can speculate that Ti, Fe, Co, Ni, Zr and Ru solutes will retard the annihilation of SFs to some extent. However, within the range of binary system, great stability of SFs cannot be reached. Correspondingly, very few 9R phases was remained in highly deformed region at room temperature<sup>46, 47, 49-51</sup>.

High concentration of segregated solutes and high ISFE retard the migration of ITBs. Desired solute elements that can act as ITB stabilizer should be strongly segregated at ITB while not apparently reduce ISFE. Fig. 8(b) shows variation of segregation energy at ITB with solute element. All studied elements could produce negative segregation energy, indicating higher solute

concentration near ITBs than in grain interior. Fig. 6(a) shows the variation of ISFE with solute element when solute concentration is 6.25 at.% and 12.5 at.%. Increasing concentration of Mg, Si, Ti and Zn solutes can continuously decrease ISFE. Therefore, Mg, Si, Ti and Zn solutes are excluded from ideal ITB stabilizer in a binary system. In Fig. 8(b), segregation energy  $\leq -0.5$  eV/atom are regarded as strongly segregating binary system<sup>114</sup>. In this sense, Fe, Co and Ni interstitials can strongly segregate at ITBs. Combining the DFT results of ISFE and segregation energy, it can be speculated that Fe, Co and Ni solutes are good stabilizers for ITBs as long as the super-saturated solid solution is preserved.

Co-sputtered Al-X alloys may not maintain super-saturation at high temperature when secondary phase forms with diffusion of solutes. Alloys with solutes that are harder to diffuse in Al solvent are more likely to maintain microstructures and mechanical properties after annealing or during loading at high temperature. Fig. 8(c) shows the variation of solute diffusion activation energy in Al solvent with solute element<sup>66</sup>. It is found that Ti, Fe, Co, Zr and Ru solutes are harder to diffuse than other solutes. Among Fe, Co and Ni solutes which can strongly segregate at ITB while do not reduce ISFE, Fe solute has the largest and Ni solute has the smallest diffusion activation energy. Therefore, it is likely that Al-Fe system is more stable than Al-Co system, and Al-Ni system at high temperature. Correspondingly, as shown in Fig. 2(f), Al-5.5Fe<sup>48</sup>, Al-5.8Co and Al-4.5Ni<sup>52</sup> alloys maintain their strength after annealing at temperature up to 553, 473 and 373 K, which is consistent with the speculation. It is noted that Al-Ti and Al-Ru system should be a candidate that is as stable as Al-Fe system at high temperature. This is because the solute diffusion activation energies of Ti, Fe and Ru solutes are large and close.

#### 4.4 Optimizing alloy design principles

Based on first principles DFT calculations, it is expected that Fe, Co and Ni solutes are exceptional for refining grain size. As for promoting formation of SFs, Fe and Ru solutes are two good candidates. At room temperature, Fe solute is better for stabilizing SFs while Fe, Co, Ni, Zr and Ru solutes are better for retarding grain coarsening. Lastly, Ti, Fe and Ru solutes are selected for service at high temperature because their large diffusion activation energies will delay the formation of secondary phase. In this sense, for Al-X binary system, Al-Fe system has high strength, great hardening rate and relatively good thermal stability simultaneously. Further improvement, i.e., on thermal stability, may need introduction of more than one solute elements.

For example, if Co and Ru solutes have weak coupling effect, sputtered Al-Co-Ru alloys may have high strength, great hardening and relatively good thermal stability because Co solute can significantly reduce grain size while Ru solute favors the formation of high density of SFs and induces relatively good thermal stability. The coupling effect between two types of solute may tailor the sputtered Al alloy. For instance, compared to Al-Fe binary alloys, Al-Fe-Ti ternary alloys maintain the high strength while improve the thermal stability<sup>48</sup>. The coupling effect between Fe and Ti solutes enhances the segregation of Fe on ITBs and lowers the solute diffusivity of both solutes, thus retarding grain coarsening and delay formation of secondary phase. What's more, the coupling effect can be utilized to overcome the shortcoming of sputtered binary Al alloys that no single solute element can significantly stabilize SFs. This will be investigated in future work.

## 5. Conclusion

Sputtering techniques can fabricate super-saturated Al-X alloys with profuse nanotwinned columnar structures, stacking faults (SFs), 9R phase bands and nanotwins in each column<sup>43-53</sup>. Compared to bulk Al alloys, co-sputtered Al-X alloys have higher strength, greater strain hardening and improved stability. In this work, we conduct DFT calculations to systematically reveal the role of co-sputtering solutes.

- Co-sputtering solutes can refine columnar grain size via increasing kinetic barrier associated with surface diffusion of Al adatoms. DFT calculations indicate that Fe, Co and Ni solutes with strong binding to Al adatoms effectively refine columnar grain size; Mg, Si, Zr, Ru and Pd solutes with moderate binding to Al adatoms refine the grain to some extent; Ti and Zn solutes with weak binding to Al adatoms have less influence on grain refinement; and Ag solutes with negative extra binding energy promotes the in-plane growth of columns. Predictions based on DFT calculations agree well with experimental results.
- Co-sputtering solutes kinetically promote formation of SFs in columns, because these metal solutes do not significantly reduce the SFE but can enhance the nucleation rate of faulted surface clusters and the energy barrier for the recovery of faulted surface clusters. DFT calculations show that all 11 tested solutes, except Si, lower excess formation energy of faulted clusters. Among them, Ti, Fe, Zr and Ru solutes can significantly reduce the excess formation energy. Meanwhile, Ti, Fe, Co, Ni, Zr, Ru and Pd solutes effectively increase the energy barrier for the recovery of faulted clusters. Fe and Ru solutes are most effective in promoting the

formation of SFs because they not only lower excess formation energy but also enhance energy barrier for the recovery of faulted surface clusters. These theoretical predictions agree well with experimental results.

- High strength and enhanced strain hardening of co-sputtered Al-X alloys are mainly ascribed to fine grain size and planar crystal defects (twin boundaries, SFs, and 9R phases), as well as their thermal stability. DFT calculations reveal a low formation energy for solute segregation in the core of Shockley partial dislocations. Correspondingly, solute segregation plays the pinning effect on the motion of dislocations, which stabilizes SFs, 9R phases and ITBs. In addition, some solutes also enhance the energy barrier for the recovery of stacking faults. As a result, some Al-X alloys show high strain hardening rate and remain their high strength at deformation temperature above 500 K. DFT calculations suggest that Fe, Co and Ni solutes can effectively pin the motion of Shockley partial dislocations and their arrays (i.e., ITBs and 9R phase). Correspondingly, Al-Fe, Al-Co and Al-Ni alloys have higher strain hardening rate than other alloys. More importantly, Al-5.5Fe, Al-5.8Co and Al-4.5Ni alloys remain high strength after annealing at temperature up to 553, 473 and 373 K, respectively. As-deposited Al-5.5Fe alloys maintain high strength at 473 K deformation temperature.

### Conflicts of interest

The authors declare no competing financial interests.

### Acknowledgement

This work is supported by the Department of Energy – Basic Energy Science (DOE Award number: DE-SC0016337). Atomistic simulations were completed utilizing the Holland Computing Center of the University of Nebraska, which receives support from the Nebraska Research Initiative.

### References

1. H.-Z. Li, H.-T. Liu, Z.-Y. Liu, H.-H. Lu, H.-Y. Song and G.-D. Wang, *Materials characterization*, 2014, **88**, 1-6.
2. R. Z. Valiev, Y. Estrin, Z. Horita, T. G. Langdon, M. J. Zechetbauer and Y. T. Zhu, *JOM*, 2006, **58**, 33-39.
3. Y. Estrin and A. Vinogradov, *Acta Materialia*, 2013, **61**, 782-817.
4. S. R. Kalidindi, C. A. Bronkhorst and L. Anand, *Journal of the Mechanics and Physics of Solids*, 1992, **40**, 537-569.
5. I. J. Beyerlein and L. S. Tóth, *Progress in Materials Science*, 2009, **54**, 427-510.
6. L. Cuddy and J. Raley, *Metallurgical Transactions A*, 1983, **14**, 1989-1995.

7. V. Tellkamp, S. Dallek, D. Cheng and E. Lavernia, *Journal of Materials Research*, 2001, **16**, 938-944.
8. P. Bhattacharjee, G. Sathiaraj, M. Zaid, J. Gatti, C. Lee, C.-W. Tsai and J.-W. Yeh, *Journal of Alloys and Compounds*, 2014, **587**, 544-552.
9. L. Bracke, K. Verbeken, L. Kestens and J. Penning, *Acta Materialia*, 2009, **57**, 1512-1524.
10. F. Lasagni, B. Mingler, M. Dumont and H. P. Degischer, *Materials Science and Engineering: A*, 2008, **480**, 383-391.
11. S. Kang, Y.-S. Jung, J.-H. Jun and Y.-K. Lee, *Materials Science and Engineering: A*, 2010, **527**, 745-751.
12. J. A. Thornton, *Journal of Vacuum Science & Technology A: Vacuum, Surfaces, and Films*, 1986, **4**, 3059-3065.
13. F. Cougnon, A. Dulmaa, R. Dedoncker, R. Galbadrakh and D. Depla, *Applied Physics Letters*, 2018, **112**, 221903.
14. S. Liu, L. Bönig, J. Detch and H. Metiu, *Physical review letters*, 1995, **74**, 4495.
15. T. Kojima, M. Mizuguchi and K. Takanashi, *Surface science*, 2014, **619**, 44-48.
16. M. C. Fallis, A. F. Wright, C. Fong and M. S. Daw, *Surface science*, 1994, **311**, L717-L723.
17. G. Antczak and G. Ehrlich, *Surface diffusion: metals, metal atoms, and clusters*, Cambridge University Press, 2010.
18. J. Hirsch and T. Al-Samman, *Acta Materialia*, 2013, **61**, 818-843.
19. J. Liu and M. Kulak, 2000.
20. D. N. Seidman, E. A. Marquis and D. C. Dunand, *Acta Materialia*, 2002, **50**, 4021-4035.
21. H. Kou, J. Lu and Y. Li, *Advanced Materials*, 2014, **26**, 5518-5524.
22. L. Jiang, H. Wen, H. Yang, T. Hu, T. Topping, D. Zhang, E. J. Lavernia and J. M. Schoenung, *Acta Materialia*, 2015, **89**, 327-343.
23. K. Youssef, R. Scattergood, K. Murty and C. Koch, *Scripta materialia*, 2006, **54**, 251-256.
24. P. V. Liddicoat, X.-Z. Liao, Y. Zhao, Y. Zhu, M. Y. Murashkin, E. J. Lavernia, R. Z. Valiev and S. P. Ringer, *Nature communications*, 2010, **1**, 1-7.
25. Y. S. Sato, S. H. C. Park and H. Kokawa, *Metallurgical and Materials Transactions A*, 2001, **32**, 3033-3042.
26. R. L. Fleisgher, *Acta metallurgica*, 1961, **9**, 996-1000.
27. J. Schiøtz and K. W. Jacobsen, *Science*, 2003, **301**, 1357-1359.
28. J. R. Trelewicz and C. A. Schuh, *Acta Materialia*, 2007, **55**, 5948-5958.
29. Z. Shan, E. Stach, J. Wiezorek, J. Knapp, D. Follstaedt and S. Mao, *Science*, 2004, **305**, 654-657.
30. N. Tsuji, Y. Ito, Y. Saito and Y. Minamino, *Scripta Materialia*, 2002, **47**, 893-899.
31. N. Tsuji, R. Ueki and Y. Minamino, *Scripta Materialia*, 2002, **47**, 69-76.
32. R. Hayes, D. Witkin, F. Zhou and E. Lavernia, *Acta Materialia*, 2004, **52**, 4259-4271.
33. F. Liu and R. Kirchheim, *Journal of crystal growth*, 2004, **264**, 385-391.
34. J. Hu, Y. Shi, X. Sauvage, G. Sha and K. Lu, *Science*, 2017, **355**, 1292-1296.
35. G.-D. Sim, J. A. Krogstad, K. M. Reddy, K. Y. Xie, G. M. Valentino, T. P. Weihs and K. J. Hemker, *Science Advances*, 2017, **3**, e1700685.
36. M. Tschopp and D. McDowell, *Philosophical Magazine*, 2007, **87**, 3147-3173.
37. O. Anderoglu, A. Misra, H. Wang and X. Zhang, *Journal of Applied Physics*, 2008, **103**, 094322.
38. X. Zhang and A. Misra, *Scripta Materialia*, 2012, **66**, 860-865.

39. R. T. Ott, J. Geng, M. F. Besser, M. J. Kramer, Y. Wang, E. Park, R. LeSar and A. H. King, *Acta Materialia*, 2015, **96**, 378-389.
40. L. Lu, Y. Shen, X. Chen, L. Qian and K. Lu, *Science*, 2004, **304**, 422-426.
41. Q. Li, S. Xue, P. Price, X. Sun, J. Ding, Z. Shang, Z. Fan, H. Wang, Y. Zhang and Y. Chen, *Nanoscale*, 2020, **12**, 1356-1365.
42. M. Chen, E. Ma, K. J. Hemker, H. Sheng, Y. Wang and X. Cheng, *Science*, 2003, **300**, 1275-1277.
43. S. Xue, Z. Fan, Y. Chen, J. Li, H. Wang and X. Zhang, *Acta Materialia*, 2015, **101**, 62-70.
44. D. Bufford, Y. Liu, J. Wang, H. Wang and X. Zhang, *Nature communications*, 2014, **5**, 4864.
45. D. Bufford, Y. Liu, Y. Zhu, Z. Bi, Q. Jia, H. Wang and X. Zhang, *Materials Research Letters*, 2013, **1**, 51-60.
46. S. Xue, Q. Li, Z. Fan, H. Wang, Y. Zhang, J. Ding, H. Wang and X. Zhang, *Journal of Materials Research*, 2018, **33**, 3739-3749.
47. Y. Zhang, S. Xue, Q. Li, C. Fan, R. Su, J. Ding, H. Wang, H. Wang and X. Zhang, *Scripta Materialia*, 2018, **148**, 5-9.
48. Q. Li, D. Xie, Z. Shang, X. Sun, J. Cho, Y. Zhang, S. Xue, H. Wang, J. Wang and X. Zhang, *Acta Materialia*, 2020, **200**, 378-388.
49. Q. Li, S. Xue, J. Wang, S. Shao, A. H. Kwong, A. Giwa, Z. Fan, Y. Liu, Z. Qi and J. Ding, *Advanced Materials*, 2018, **30**, 1704629.
50. S. Xue, Q. Li, D. Xie, Y. Zhang, H. Wang, H. Wang, J. Wang and X. Zhang, *Materials Research Letters*, 2019, **7**, 33-39.
51. Y. Zhang, Q. Li, S. Xue, J. Ding, D. Xie, J. Li, T. Niu, H. Wang, H. Wang and J. Wang, *Nanoscale*, 2018, **10**, 22025-22034.
52. Y. Zhang, R. Su, D. Xie, T. Niu, S. Xue, Q. Li, Z. Shang, J. Ding, N. Richter and J. Wang, *Nanoscale*, 2020, **12**, 20491-20505.
53. N. Richter, Y. Zhang, D. Xie, R. Su, Q. Li, S. Xue, T. Niu, J. Wang, H. Wang and X. Zhang, *Materials Research Letters*, 2020, **9**, 91-98.
54. J. Musil, M. Šašek, P. Zeman, R. Čerstvý, D. Heřman, J. Han and V. Šatava, *Surface and Coatings Technology*, 2008, **202**, 3485-3493.
55. D. K. Merl, P. Panjan and J. Kovač, *Corrosion science*, 2013, **69**, 359-368.
56. A. E. Lita and J. E. Sanchez Jr, *Journal of applied physics*, 1999, **85**, 876-882.
57. Q. Li, Z. Shang, X. Sun, C. Fan, R. Su, N. A. Richter, Z. Fan, Y. Zhang, S. Xue and H. Wang, *International Journal of Plasticity*, 2021, **137**, 102915.
58. V. C. Gudla, K. Rechendorff, Z. I. Balogh, T. Kasama and R. Ambat, *Materials & Design*, 2016, **89**, 1071-1078.
59. M. Draissia, H. Boudemagh and M. Debli, *Physica Scripta*, 2004, **69**, 348.
60. M. Bielawski, *Surface and Coatings Technology*, 2004, **179**, 10-17.
61. J. Wang, N. Li and A. Misra, *Philosophical Magazine*, 2013, **93**, 315-327.
62. D. Ma, M. Friák, J. von Pezold, J. Neugebauer and D. Raabe, *Acta Materialia*, 2015, **98**, 367-376.
63. Y. Tian, L. Zhao, S. Chen, A. Shibata, Z. Zhang and N. Tsuji, *Scientific reports*, 2015, **5**, 16707.
64. L. Lu, X. Chen, X. Huang and K. Lu, *Science*, 2009, **323**, 607-610.
65. Z. Wu, Y. Zhang and D. Srolovitz, *Acta Materialia*, 2009, **57**, 4508-4518.
66. D. Simonovic and M. H. Sluiter, *Physical Review B*, 2009, **79**, 054304.

67. G. Kresse and J. Furthmüller, *Computational materials science*, 1996, **6**, 15-50.
68. G. Kresse and D. Joubert, *Physical review b*, 1999, **59**, 1758.
69. J. P. Perdew, K. Burke and M. Ernzerhof, *Physical review letters*, 1996, **77**, 3865.
70. P. E. Blöchl, *Physical review B*, 1994, **50**, 17953.
71. H. J. Monkhorst and J. D. Pack, *Physical review B*, 1976, **13**, 5188.
72. P. Janthon, S. Luo, S. M. Kozlov, F. Vines, J. Limtrakul, D. G. Truhlar and F. Illas, *Journal of chemical theory and computation*, 2014, **10**, 3832-3839.
73. G.-X. Zhang, A. M. Reilly, A. Tkatchenko and M. Scheffler, *New Journal of Physics*, 2018, **20**, 063020.
74. L. Schimka, R. Gaudoin, J. Klimeš, M. Marsman and G. Kresse, *Physical Review B*, 2013, **87**, 214102.
75. M.-P. Delplancke-Ogletree, in *Materials Surface Processing by Directed Energy Techniques*, Elsevier, 2006, pp. 383-410.
76. C. Liu, J. Cohen, J. Adams and A. Voter, *Surface Science*, 1991, **253**, 334-344.
77. R. Stumpf and M. Scheffler, *Physical Review Letters*, 1994, **72**, 254.
78. R. Stumpf and M. Scheffler, *Physical Review B*, 1996, **53**, 4958.
79. C. Busse, W. Langenkamp, C. Polop, A. Petersen, H. Hansen, U. Linke, P. J. Feibelman and T. Michely, *Surface Science*, 2003, **539**, L560-L566.
80. T. Michely, W. Langenkamp, H. Hansen and C. Busse, *Physical Review Letters*, 2001, **86**, 2695.
81. S. Ovesson, A. Bogicevic, G. Wahnström and B. I. Lundqvist, *Physical Review B*, 2001, **64**, 125423.
82. C. Polop, H. Hansen, W. Langenkamp, Z. Zhong, C. Busse, U. Linke, M. Kotrla, P. J. Feibelman and T. Michely, *Surface Science*, 2005, **575**, 89-102.
83. C. Chang, C. Wei and S. Chen, *Physical Review Letters*, 2000, **85**, 1044.
84. C. Chang, C. Wei and S. Chen, *Surface Science*, 2000, **465**, 65-75.
85. H. Frost, C. Thompson and D. Walton, *Acta Metallurgica et Materialia*, 1990, **38**, 1455-1462.
86. H. Frost, C. Thompson and D. Walton, *Acta metallurgica et materialia*, 1992, **40**, 779-793.
87. M. Legros, D. S. Gianola and K. J. Hemker, *Acta Materialia*, 2008, **56**, 3380-3393.
88. T. Rupert, D. Gianola, Y. Gan and K. Hemker, *Science*, 2009, **326**, 1686-1690.
89. C. V. Thompson and R. Carel, *Journal of the Mechanics and Physics of Solids*, 1996, **44**, 657-673.
90. L. Vitos, A. Ruban, H. L. Skriver and J. Kollar, *Surface Science*, 1998, **411**, 186-202.
91. R. Kirchheim, *Acta Materialia*, 2002, **50**, 413-419.
92. M. Aoki, Y. M. Chiang, I. Kosacki, L. J. R. Lee, H. Tuller and Y. Liu, *Journal of the American ceramic society*, 1996, **79**, 1169-1180.
93. H. Aaron and G. Bolling, *Surface Science*, 1972, **31**, 27-49.
94. A. Bogicevic, J. Strömquist and B. I. Lundqvist, *Physical Review Letters*, 1998, **81**, 637.
95. O. Trushin, K. Kokko, P. Salo, W. Hergert and M. Kotrla, *Physical Review B*, 1997, **56**, 12135.
96. L. Kong and L. J. Lewis, *Physical Review B*, 2008, **77**, 165422.
97. M. Karimi, T. Tomkowski, G. Vidali and O. Biham, *Physical Review B*, 1995, **52**, 5364.
98. J. Ferrón, L. Gómez, J. de Miguel and R. Miranda, *Physical Review Letters*, 2004, **93**, 166107.

99. J. Barth, H. Brune, B. Fischer, J. Weckesser and K. Kern, *Physical Review Letters*, 2000, **84**, 1732.
100. W. Wulfhekel, N. N. Lipkin, J. Kliewer, G. Rosenfeld, L. C. Jorritsma, B. Poelsema and G. Comsa, *Surface Science*, 1996, **348**, 227-242.
101. J. Repp, F. Moresco, G. Meyer, K.-H. Rieder, P. Hyldgaard and M. Persson, *Physical Review Letters*, 2000, **85**, 2981.
102. N. Knorr, H. Brune, M. Epple, A. Hirstein, M. Schneider and K. Kern, *Physical Review B*, 2002, **65**, 115420.
103. A. B. Hamouda, R. Sathiyarayanan, A. Pimpinelli and T. Einstein, *Physical Review B*, 2011, **83**, 035423.
104. J. Venables, *Physical Review B*, 1987, **36**, 4153.
105. R. Sathiyarayanan, A. B. Hamouda, A. Pimpinelli and T. Einstein, *Physical Review B*, 2011, **83**, 035424.
106. Y. Qi and R. K. Mishra, *Physical Review B*, 2007, **75**, 224105.
107. D. Zhang and R. Picu, *Modelling and Simulation in Materials Science and Engineering*, 2003, **12**, 121.
108. S. Zhao, Y. Osetsky, G. M. Stocks and Y. Zhang, *npj Computational Materials*, 2019, **5**, 1-7.
109. C. Busse, C. Polop, M. Müller, K. Albe, U. Linke and T. Michely, *Physical Review Letters*, 2003, **91**, 056103.
110. C. Polop, A. Lammerschop, C. Busse and T. Michely, *Physical Review B*, 2005, **71**, 125423.
111. H. Chu, H. Huang and J. Wang, *Scientific Reports*, 2017, **7**, 5167.
112. S. I. Shah, G. Nandipati, A. Kara and T. S. Rahman, *Physical Review B*, 2013, **88**, 035414.
113. J. Wang, N. Li, O. Anderoglu, X. Zhang, A. Misra, J. Huang and J. Hirth, *Acta Materialia*, 2010, **58**, 2262-2270.
114. J. R. Trelewicz and C. A. Schuh, *Physical Review B*, 2009, **79**, 094112.
115. N. A. Belov, D. G. Eskin and A. A. Aksenov, *Multicomponent phase diagrams: applications for commercial aluminum alloys*, Elsevier, 2005.